Gust mitigation through closed-loop control. I. Trailing-edge flap response

Johannes E. Pohl, Rolf Radespiel, Benjamin Herrmann, Steven L. Brunton, and Richard Semaan

Phys. Rev. Fluids **7**, 024705 — Published 10 February 2022

DOI: 10.1103/PhysRevFluids.7.024705

Gust mitigation through closed-loop control. Part I: Trailing-edge flap response

Johannes E. Pohl, Rolf Radespiel
Institute of Fluid Mechanics, Technische Universität Braunschweig, Braunschweig, 38106, Germany

Benjamin Herrmann
Department of Mechanical Engineering, Universidad de Chile, Beauchef 851, Santiago, Chile

Steven L. Brunton
Department of Mechanical Engineering, University of Washington, Seattle, WA 98195, USA

Richard Semaan*
Institute of Fluid Mechanics, Technische Universität Braunschweig, Braunschweig, 38106, Germany

(Dated: January 7, 2022)

We quantify and model the airfoil response to its pitching flap using a comprehensive experimentally-acquired database at chord-based Reynolds number $1.8 \cdot 10^6$. This quantification relies on two newly proposed metrics that characterize the dynamic lift hysteresis and allow describing its evolution under different pitching conditions. The analysis reveals a saturation of the relative lift hysteresis that is independent of the angle of attack. Moreover, the hysteresis loop is shown to reach phase opposition at the same reduced frequency as when its tilt slope begins to change direction. The two-pronged characterization of the lift hysteresis a promising new approach to quantify the unsteady aerodynamic behavior beyond the reported conditions and of other immersed bodies. The modeling strategy yields one nonlinear model and a set of linear models. The models' performance is examined under a range of flow and pitching conditions. Despite their reduced accuracy compared to the nonlinear model, the linear models are chosen to be incorporated in the closed-loop control strategy that we detail in Part II of this series.

I. INTRODUCTION

Gust mitigation is relevant to a range of engineering applications, such as passenger aircraft, wind turbines, and micro-air vehicles. Without counter-measures, gust encounters can lead to extreme loads on the structure and to possible loss of control. Due to its relevance, various actuation concepts have been investigated to counter gust effects. These include blown jets [1], synthetic jets [2], and control surfaces [3] among others. In this project, we employ a trailing edge flap for active control with the objective of regulating lift during a gust encounter. This is implemented using a model-based closed-loop control strategy. A first step in achieving this objective is the quantification and the modeling of the lift response to the pitching flap, which we present in this first paper of the series.

The foundations of the classical theory of unsteady aerodynamics can be traced back to Prandtl [4] and Birnbaum [5] in 1924. Their formulation was expanded by Wagner [6] in 1925 to solve the indicial problem, representing the aerodynamic response to an arbitrary wing motion as the convolution of the motion with the aerodynamic response to an impulsive motion. A solution to the frequency response problem was presented in 1935 by Theodorsen [7], which was subsequently generalized by Von Karman and Sears [8] in 1938. Since these seminal works, multiple expansions and approximations in the time [9] and in frequency [10] space have been introduced. As long as the flow over an airfoil remains attached, these 'classical' models have been shown to deliver good load predictions [11]. However, for large angle of attack variations, where dynamic stall might occur, these models become increasingly less accurate [12]. This is mainly caused by the neglected viscous effects that manifest themselves through local separations and leading-edge vortex [13]; vortex modeling approaches provide a flexible approach to capture many of these effects [14–16].

To address these shortcomings, many studies adopted data-driven modeling approaches. Some maintained the same Theodorsen's model structure and identified an *empirical* Theodorsen function using either experimental [11] or numerical [17, 18] data. Alternative data-driven modeling approaches abandon Theodorsen's model structure for a heuristic one. These include the Snel [19], the Goman-Khrabrov [20–22], the ONERA [23], and other heuristic [24] models. Despite their broader applicability range in comparison to the classical methods, many of these data-driven models are not well-generalizable to different airfoil geometries or different operating conditions, unless parameter variations are specifically accounted for [25]. Moreover, the majority of unsteady aerodynamic models have been

---

* r.semaan@tu-bs.de

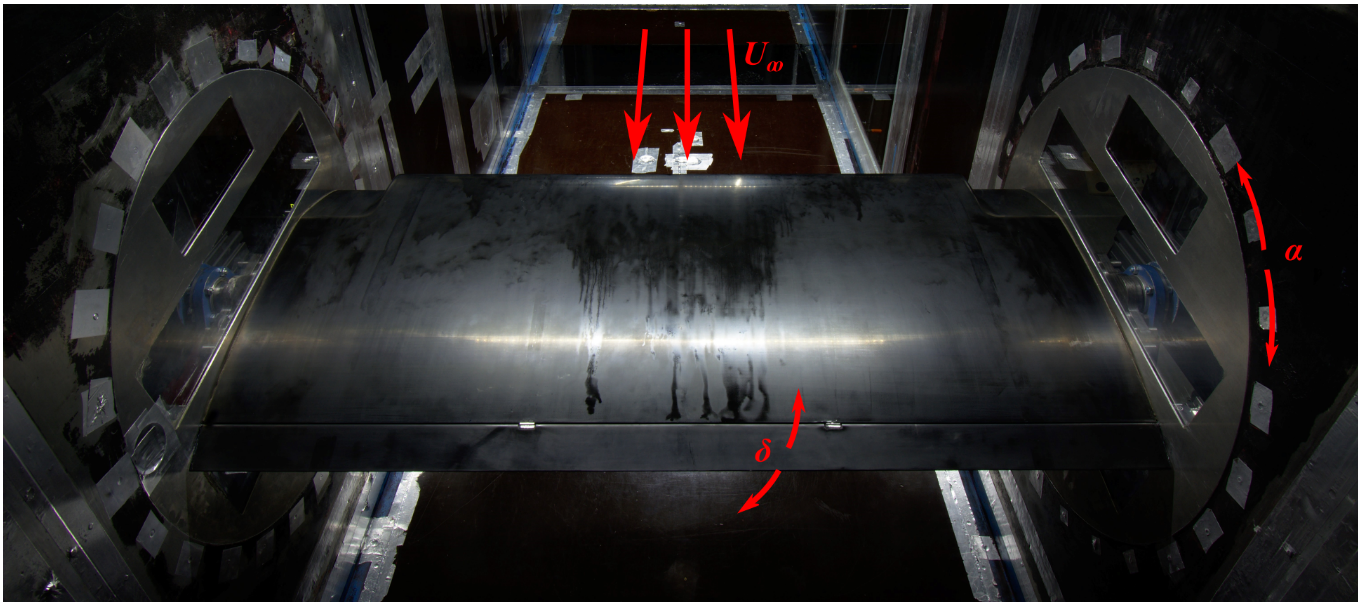

FIG. 1. The DLR-F15 research airfoil inside the MUB wind tunnel. Also shown is the incident flow U_∞, the angular traversing mechanism of the airfoil angle of attack α, and the flap angle δ.

constructed and validated at relatively low Reynolds numbers on the order of $Re = 5 \cdot 10^4$ or lower [26–28], which is representative of the fluid dynamics for micro-air vehicles. With few exceptions (e.g., [29]), high Reynolds number studies, which are particularly relevant to passenger aircraft, are largely absent from the literature.

One defining attribute of unsteady aerodynamics is the lift hysteresis, whose characteristics depend on the pitch settings. Lift hysteresis results from the phase lead of noncirculatory flow effects and the phase lag due to vorticity convection into the wake. While non-circulatory effects are negligible at low reduced frequencies, they become progressively larger with increasing pitch rate until they become dominant at sufficiently high reduced frequency. The reduced frequency is the non-dimensional pitching frequency scaled with the free-stream velocity and the airfoil half-chord. Panda and Zaman [30] reported the shape similarity of the hysteresis loop at varying oscillation amplitude for a given frequency. They claimed that only the size of the loop varied proportionally to the amplitude. The Mach number effects on the lift hysteresis were investigated in Hariharan and Leishman [31], where an increase in circulatory lag was observed with increasing Mach number. Recent findings by Williams et al. [32] indicate that dynamic hysteresis in separated flows depends primarily on the pitch motion, $\alpha(t)$, the pitch rate, $\dot{\alpha}(t)$, and the amount of flow attachment on the airfoil. The authors report dynamic hysteresis even at relatively small pitch rates, which suggests that the concentrated dynamic stall vortex observed at high reduced frequency is not a requirement for dynamic hysteresis. These aforementioned studies and others have shed light on the dynamic lift hysteresis phenomenon. However, no known attempt has been reported on quantifying it over a range of conditions, particularly at high Reynolds numbers.

In this study, we aim to address this gap in the literature by performing a comprehensive experimental study at a chord Reynolds number $Re_c = 1.8 \cdot 10^6$ on an airfoil with a pitching flap. The acquired dataset is used to quantify and analyze the lift hysteresis over a broad range of pitching conditions. Two models of the unsteady lift coefficient are constructed, compared, and assessed for their suitability for gust mitigation within a model-based closed-loop control strategy, which is presented in Part II of this series.

II. EXPERIMENTAL SETUP

A. Wind tunnel facility and experimental model

The experiment is conducted in the Modell-Unterschallkanal Braunschweig (MUB) wind tunnel at the Institute of Fluid Mechanics of the Technische Universität Braunschweig. The MUB is a low-speed closed-circuit wind tunnel with a 1.3 m × 1.3 m × 5.7 m test section. Flow speeds of up to 60 m/s can be achieved in the test section. In the current experiment, the incident flow is maintained at a constant velocity of $U_\infty = 50\,\mathrm{m/s}$ and a constant temperature of $\approx 36\,^\circ\mathrm{C}$. The airfoil in the wind tunnel test section is shown in Fig. 1, whereas Fig. 2 illustrates the setup and presents the relevant geometric variables. The DLR-F15 airfoil has a span of 1.3 m and a chord length of $c = 600\,\mathrm{mm}$,

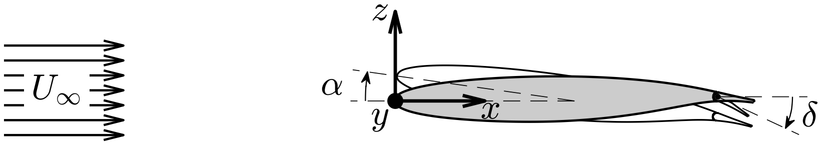

FIG. 2. Schematics of the DLR-F15 research airfoil with the pitching flap. The airfoil angle of attack α and flap angle δ are defined positive in the clockwise direction with incident flow from the left.

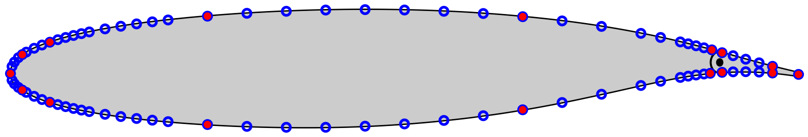

FIG. 3. Pressure sensor distribution over the DLR-F15 airfoil midspan. Blue circles indicate steady pressure taps, whereas red dots represent time-resolved pressure measurement locations.

resulting in a chord Reynolds number $Re_c \approx 1.8 \cdot 10^6$. The model leading edge is gradually drooped near the two sidewalls for a span length of 130 mm to minimize wind tunnel boundary layer effects along the midsection at high angles of attack. The airfoil is equipped with a trailing edge flap adapted from the clean airfoil configuration with a chord length of $c_\mathrm{F} = 0.1 \cdot c = 60\,\mathrm{mm}$. A gap of approximately 1 mm between the main airfoil trailing edge and the flap leading edge allows free rotation. No sealing is applied across the gap. While the main body is made of a glass fiber composite (GFC) shell glued to an aluminum frame, the flap is constructed from carbon fiber composite (CFC) with several stiffening elements to withstand the actuation torque and unsteady loads. Two ESR Pollmeier MH4251 servo motors with a nominal torque of 14 N m each and an electric time constant $\tau_\mathrm{el} = 1.12\,\mathrm{ms}$ are used to deflect the flap by up to $\delta = \pm 25\,^\circ$. Both motors are connected to the flap's integrated drive elements with safety clutches to prevent overload. Additional mechanical safety stoppers are built-in to help avoid collisions between the flap and the airfoil main body. The servo controllers are commanded by the main data acquisition and control system through a NI cRIO-9039 FPGA controller.

One part of the experimental setup, which is relevant in Part II of the series, is the gust generator mechanism that is situated $\approx 2.5\,\mathrm{m}$ upstream of the DLR-F15 research airfoil. Details on the gust generator setup are not presented in this paper. We only note that for the 'parked' position at zero angle of attack, the gust generator airfoil wake generates small flow disturbances on the research airfoil. These small disturbances are likely to affect the flow response. However, it is beneficial to include them in the model-training phase for a more robust model and subsequently a more robust closed-loop control. Details on the gust generator setup and its effects on the research airfoil are provided in Part II.

B. Acquisition and control systems

In this study, we investigate the unsteady lift of the pitching flap under various conditions. This requires real-time determination of the lift force, which we achieve using a mapping technique [33, 34] based on 16 time-resolved and 84 steady pressure sensors located along the airfoil midspan (c.f. Fig. 3). This mapping is necessary to correct for the relatively coarse pressure distribution obtained from the time-resolved pressure sensors (red dots in Fig. 3). The mapping relies on piecewise correction of the unsteady surface pressure to the closest steady curve segment from a large library of distributions.

The steady pressure taps with 0.3 mm diameter are connected to a DTC Initium system with calibrated ESP-HD type pressure scanners with $\pm 0.05\,\%$ full-scale accuracy. The Honeywell SDX05D4 fast pressure sensors acquire the surface pressure through $50 - 150\,\mathrm{mm}$ long and 0.8 mm diameter tubes. In-situ step response tests of the Honeywell sensors have shown negligible time delay and signal distortion in the frequency range of interest. The transducers feature passive temperature compensation, and a live offset adjustment ensures matching pressures between the time-resolved and the steady pressure sensors.

The second type of measured data is the flap angular position, which is acquired by two Sick DFS60 differential position encoders with a 20" resolution installed on the two flap driveshafts so that the flap position can be acquired directly without the need to account for twist in the safety clutches.

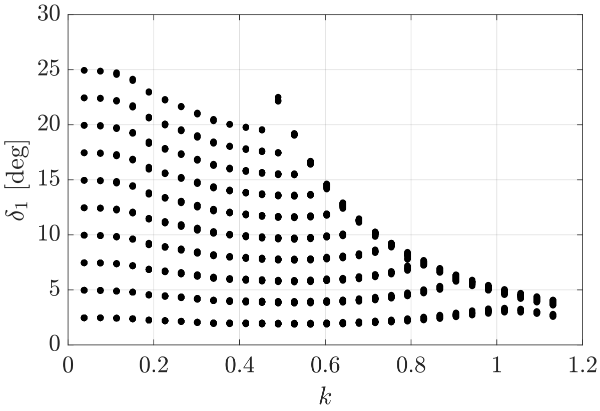

FIG. 4. Visual summary of the test cases for $\alpha = 0\,^\circ$. Similar parametric coverage is achieved for $\alpha = 5\,^\circ$ and $8\,^\circ$.

All acquisition and control processes are centrally managed by a LabVIEW code running on the FPGA of the cRIO-9039 at a rate of 100 kHz, which ensures that all data and tasks are processed in real-time. The code controls all data acquisition, initial processing, and control tasks autonomously on the FPGA. The live sampled data is transmitted to a host PC for monitoring and recording.

C. Test cases

The flow response to the pitching flap is quantified through a parametric study of harmonic oscillation, which is defined as:

$$\delta(t^*) = \delta_0 + \delta_1 \sin(k\, t^*), \tag{1}$$

where $\delta_0 = (\delta_{\max} + \delta_{\min})/2$ represents the mean pitch angle, $\delta_1 = (\delta_{\max} - \delta_{\min})/2$ represents the pitch amplitude, $k = \omega\, c/2\, U_\infty$ is the reduced frequency of oscillation, and $t^* = 2t\, U_\infty/c$ is the convective time. The minimum and maximum flap angle are varied between $\delta_{\min}, \delta_{\max} \in [-25\,^\circ,\ 25\,^\circ]$ in steps of $5\,^\circ$, yielding a good coverage of the parameter space. Similarly, the reduced frequency is varied in the range $k \in [0,\ 1.131]$ in intervals of 0.038. This yields a total of 1650 test cases at each angle of attack. Measurements are acquired at three angles of attack $\alpha = 0, 5, 8\,^\circ$. To reduce the measurement uncertainty, each test case is sampled over 60 cycles and phase-averaged over the middle 50 periods [35]. In other words, the first and last 5 periods are neglected to exclude possible transient effects between test cases.

Due to electromechanical limitations in the flap acceleration rate, not all desired pitch amplitudes are attained. The measured test cases at $\alpha = 0\,^\circ$ are summarized in Fig. 4. As the figure shows, there is a clear decrease in the achieved pitch amplitude with increasing frequency. Also observed is the 'saturation front' of the servo motor, where certain $\delta_1 - k$ combinations remain out of reach. Similar parametric coverage and behavior is achieved for $\alpha = 5\,^\circ$ and $8\,^\circ$.

III. MODELING OF THE UNSTEADY AIRFOIL LIFT

An important component of our overall active gust mitigation strategy is the flow response model. Specifically, we seek an accurate and simple model of the lift coefficient response to flap deflections. Besides better interpretability, simplicity is motivated by the desire to employ low-latency control. In this section, we present two modeling approaches. The first nonlinear model is developed in the time domain and is based on a simplified version of the ONERA model. The second set of linear models is directly identified from a data subset in the frequency domain.

TABLE I. List of the model coefficients identified from the measurement data.

ξ_0	ξ_1	ξ_2	C_L^0	a_1	d_1	d_2	d_3	d_4
-1.967	1.615	0.159	0.200	6.487	1.610	-1.382	-1.422	3.851

A. Nonlinear model

The ONERA model [23] constitutes the starting point of our first modeling strategy. The model considers two lift coefficient components

$$C_L = C_{L,1} + C_{L,2}\,, \tag{2}$$

where the evolution of $C_{L,1}$ and $C_{L,2}$ is determined by two differential equations,

$$\dot{C}_{L,1} + \lambda C_{L,1} = \lambda C_{L,\mathcal{L}} + (\lambda\zeta + \sigma)\,\dot{\delta} + \zeta\ddot{\delta} \tag{3}$$

$$\ddot{C}_{L,2} + a\dot{C}_{L,2} + rC_{L,2} = -\left(r\Delta + e\dot{\Delta}\right)\,, \tag{4}$$

where the variable $C_{L,\mathcal{L}}$ is a linear extrapolation of the static lift C_L^{s}, and $\Delta = C_{L,\mathcal{L}} - C_L^{\mathrm{s}}$ is the difference between this extrapolation and the actual static curve. The coefficients λ, σ, and ζ are constants that depend on the airfoil geometry and the Reynolds number. This means that a separate set of these coefficients is required for different airfoil and flow conditions, which limits the generalizability of the model. a, r and e are functions of Δ, as follows

$$r = \left[r_0 + r_2\,(\Delta)^2\right]^2, \quad a = a_0 + a_2\,(\Delta)^2, \quad e = e_2\,(\Delta)^2\,. \tag{5}$$

The coefficients a_0, a_2, r_0, r_2 and e_2 are identified from wind tunnel measurements.

The structure of the two differential equations, Eq. (3) and Eq. (4), is not arbitrary. When pitching below the onset of stall, the unsteady lift can be described by the first-order differential equation, Eq. (3), having a single real and negative pole. On the other hand, in the presence of stall, description of the lift evolution also requires the second-order differential equation, Eq. (4), adding two complex conjugate poles. This explains the two lift components in Eq. (2), where one is governed by the first-order equation and the other by the second-order equation.

The ONERA model yields a good prediction accuracy and is often the method of choice for modeling unsteady aerodynamic loads [36, 37]. However, our closed-loop control strategy favors simple models. As such, the ONERA model is simplified by assuming negligible dynamic stall and hence eliminating Eq. (4) entirely. The validity of this assumption is verified a posteriori in the results, where the relatively small flap is shown to generate no or small dynamic stall at $\alpha \lessapprox 12\,^\circ$. The retained ONERA model given by Eq. (3) can be expressed as

$$\xi_0\dot{C}_L + C_L = C_L^{\mathrm{s}} + \xi_1\dot{\delta} + \xi_2\ddot{\delta}\,, \tag{6}$$

where the dot represents differentiation with respect to the convective time $(\dot{\ }) = d(\ )/dt^*$, and ξ_i are the model coefficients. We emphasize that only the structure of Eq. (3) is retained and the model coefficients are identified from the measurement data. The steady lift coefficient C_L^{s} is modeled separately as a fourth-order polynomial:

$$C_L^{\mathrm{s}}(\alpha,\delta) = C_L^0 + a_1\alpha + d_1\delta + d_2\delta^2 + d_3\delta^3 + d_4\delta^4\,. \tag{7}$$

The model coefficients for Eq. (6) and Eq. (7) are identified from the data using a least-squares fit. The coefficients are listed in table I.

The model's accuracy is quantified using the root-mean-square error between the model predictions and the measured reference data,

$$E_{\mathrm{rms}} = \sqrt{\frac{1}{N}\sum_{i=1}^{N}(\Delta C_{L,i})^2}\,, \tag{8}$$

where N is the total number of samples for one test case, and $\Delta C_{L,i}$ denotes the difference between the model and the reference lift coefficient. The averaged root mean square error over *all test cases* amounts to 0.025 for the static Eq. (7) and 0.011 for the dynamic Eq. (6) model components, indicating a good prediction accuracy. A detailed assessment of the model prediction capabilities is provided in section IV C.

TABLE II. Identified coefficients for the linear models given by Eq. (12) at various airfoil angles of attack α.

α	a_0	a_1	a_2	b_0	b_1	b_2
0 deg	1.93485	5.13803	1.41021	1.107	5.793	1.000
5 deg	3.29235	7.65731	1.59824	2.029	8.652	1.000
8 deg	0.53078	1.34597	1.00432	0.369	1.451	1.000

B. Linear models

A second modeling strategy generates a set of linear models that are amenable to closed-loop control. The models' structure is inspired by Theodorsen's solution. Following Leishman [38, 39], the unsteady lift on an airfoil with a harmonically pitching flap in incompressible flow is given by

$$C_L(k) = 2\pi\alpha + c_1\dot{\delta} + c_2\ddot{\delta} + \left(c_3\delta + c_4\dot{\delta}\right)C(k), \tag{9}$$

where $C(k)$ is the Theodorsen's transfer function that accounts for attenuation of the circulatory lift by the wake vorticity, given by

$$C(k) = \frac{H_1^{(2)}(k)}{H_1^{(2)}(k) + iH_0^{(2)}(k)}, \tag{10}$$

where $H_\nu^{(2)}$ are Hankel functions of the second kind. The coefficients c_i in Eq. (9) depend only on the distance between the flap hinge and the mid-chord, e, as follows

$$c_1 = \cos^{-1}(e) - e\sqrt{1-e^2}, \tag{11a}$$

$$c_2 = \tfrac{1}{3}(2+e^2)\sqrt{1-e^2} - e\cos^{-1}(e), \tag{11b}$$

$$c_3 = 2\sqrt{1-e^2} + 2\cos^{-1}(e), \tag{11c}$$

$$c_4 = (1-2e)\cos^{-1}(e) + (2-e)\sqrt{(1-e^2)}, \tag{11d}$$

where e is measured in semi-chords. In our experimental setup with $e = 0.8$, the contribution of the terms multiplying c_1, c_2, and c_4 is therefore small relative to the c_3 term for the range of frequencies studied. More specifically, these terms are an order of magnitude smaller than c_3k for frequencies of $k \sim O(1)$. Consequently, a transfer function with δ as the input and $C_L - 2\pi\alpha$ as the output will yield the same structure as $C(k)$. Theodorsen's transfer function has been historically approximated by rational functions with the same number of poles and zeros to preserve the constant value asymptotes that $C(k)$ exhibits for both low and high frequencies [17, 18]. Therefore, we expect a proper, rather than strictly proper, transfer function to be able to explain the experimental data for reduced frequencies $k < 1$ and small pitching amplitudes. For an empirical model based on data at higher frequencies, we would not expect the high-frequency asymptote of $C(k)$ to be respected since it describes an instantaneous change in the circulatory lift in response to changes in δ, which is nonphysical [40, 41]. Moreover, the added mass terms contribution becomes significant at higher frequencies. Therefore, modeling would require considering the flap pitch rate $\dot{\delta}$ or acceleration $\ddot{\delta}$ as the input rather than the pitch angle δ to produce a strictly proper transfer function for the unsteady lift.

In addition to enabling a direct comparison with thin airfoil theory, working in the frequency domain is motivated by the characteristics of our harmonic forcing, which we convert to the frequency domain via a Fourier transform. For each of the three models at the three angles of attack, training is performed on a data subset at a single mean pitch angle $\delta_0 = 0°$, and a range of pitching amplitudes $\delta_1 < 10°$, and reduced frequencies $k < 0.75$. This range is well within the requirements to mitigate the largest vortex gusts generated by the facility. Transfer function models are fit to the frequency response data for every angle of attack using MATLAB's `tfest` command [42]. Different combinations of the number of poles and zeros are tested and the least complex models that accurately fit the data are transfer functions with two poles and two zeros with the following structure

$$G(s) = \frac{a_2s^2 + a_1s + a_0}{b_2s^2 + b_1s + b_0}, \tag{12}$$

where $s = k/(2\pi)$ is in reduced frequency units. The identified coefficients in Eq. (12) are listed in Table II for the three angles of attack. The mean square error between data and models is below $5 \cdot 10^{-4}$ for all three models.

The frequency response of the linear models, as well as that from the theory using Eq. (9), are compared to the experimental data in Fig. 5. The linear models not only accurately fit the data, but also share the structure of

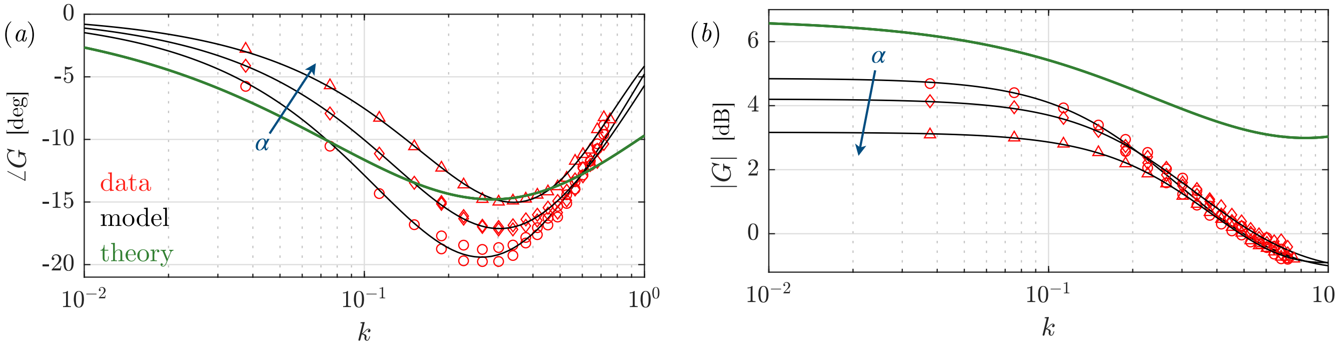

FIG. 5. Frequency response of the linear models given by Eq. (12) at airfoil angles of attack $\alpha \in \{0°, 5°, 8°\}$, along with experimental data for $\delta_1 < 10°$ and predictions from thin airfoil theory according to Eq. (9): (*a*) Phase. (*b*) Magnitude. The symbols denote the three angles of attack for the experimental distributions.

theoretical approximations by having the same number of poles as zeros. Because of this structure, the models have constant value asymptotes at low and high frequencies given by a_0/b_0 and a_2/b_2, respectively. The low-frequency asymptote corresponds to the *dc gain*, representing the increment in the static lift in response to an increment in the flap deflection angle. The *dc gain* is found to decrease when increasing the airfoil angle of attack, as shown in Fig. 5(*b*), which we ascribe to the reduction in the control authority of the flap with increasing flow separation. The high-frequency gains represent an instantaneous increment in the unsteady lift when increasing δ, as predicted by the thin-airfoil theory. Since our models are identified using data for $k < 0.75$, the produced high-frequency gains might be misleading, and we refrain from interpreting them. An assessment of the predictive performance of the models is presented in section IV C. Note that it is possible to combine several linear models at different operating conditions into a parameter-varying model that is suitable for control and accurate over a larger envelope [25, 43].

IV. RESULTS AND DISCUSSION

A. Steady lift

In this section, we examine the steady lift behavior of the research airfoil measured at various angles of attack and flap deflection angles. The steady airfoil lift coefficient distribution C_L^{s} is shown in Fig. 6(*a*) for an angle of attack α range at a constant flap angle of $\delta = 0°$. The linear region closely approximates the potential flow solution and extends with a 2π slope from the lower end of the measured range at $\alpha = -6°$ up to $\alpha = 8°$. For higher angles of attack, separation effects begin to take hold over the airfoil suction side, leading to a decrease in the lift slope $\mathrm{d}C_L^{\mathrm{s}}/\,\mathrm{d}\alpha$ and a resulting maximum lift coefficient $C_L^{\max} = 1.55$ at $\alpha = 20°$.

The steady airfoil lift distributions for varying flap deflection angle $\delta \in [-25°, 25°]$ are presented in Fig. 6(*b*) for the three angles of attack. All three distributions exhibit a similar trend. They are shifted with respect to one another by a constant over the entire range of flap deflection angles. This similarity is expected, as all three angles of attack reside in the linear range below static stall. Also shown in the figure are the corresponding static fit models given by Eq. (7), which match the reference distributions accurately. Using the surface pressure measurements over the flap, we divide the flow into three states. A quasi-linear behavior is observed between $\delta_{\mathrm{sep}}^{-} = -20°$ and $\delta_{\mathrm{sep}}^{+} = 5°$, which delimits the attached flow region over the flap pressure and suction side, respectively. The asymmetry in the separation range with respect to zero is simply due to the asymmetry of the airfoil geometry. For $\delta < -20°$, the flow over the flap pressure side starts to separate, resulting in a decreasing gradient $\mathrm{d}C_L^{\mathrm{s}}/\,\mathrm{d}\delta$. Similarly, for $\delta > 15°$, $\mathrm{d}C_L^{\mathrm{s}}/\,\mathrm{d}\delta$ decreases due to the onset of flow separation over the flap suction side. No separation of the main element is observed across the measured angle of attack range $\alpha \in [0°, 8°]$.

B. Unsteady lift and hysteresis quantification

The unsteady lift response under harmonic pitching of the trailing-edge flap is investigated in this section. We first examine the surface pressure distributions, which are presented in Fig. 7 for three reduced frequencies k during the flap upstroke (denoted by [−] in Figs. 7(*a*)-(*c*)) and downstroke (denoted by [+] in Figs. 7(*d*)-(*f*)) at $\delta = 0°$. The

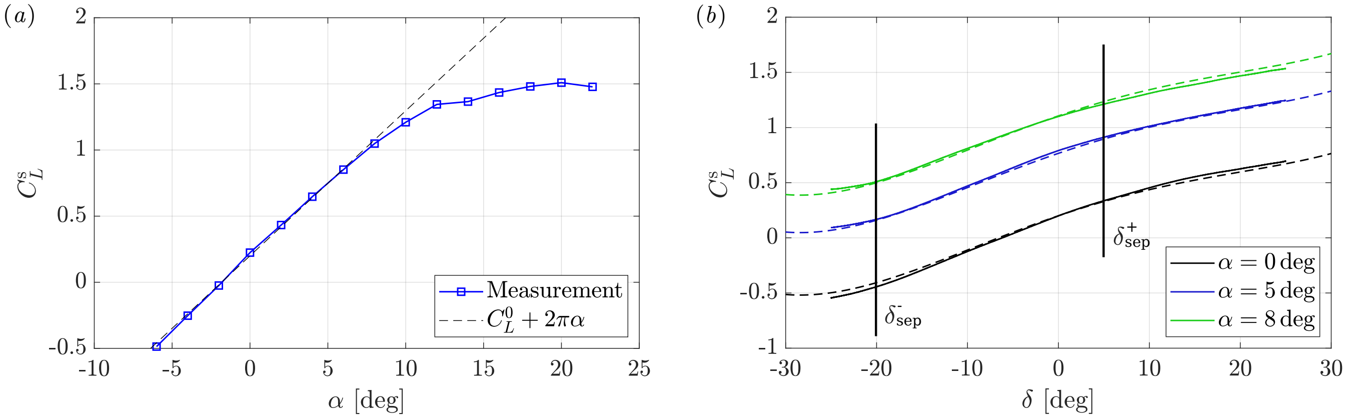

FIG. 6. (*a*) Steady lift coefficient distribution over an angle of attack range α at $\delta_0 = 0°$. (*b*) Steady lift coefficient distributions for flap deflection angle variations δ at three angles of attack. The dashed lines denote the corresponding polynomial model given by Eq. (7).

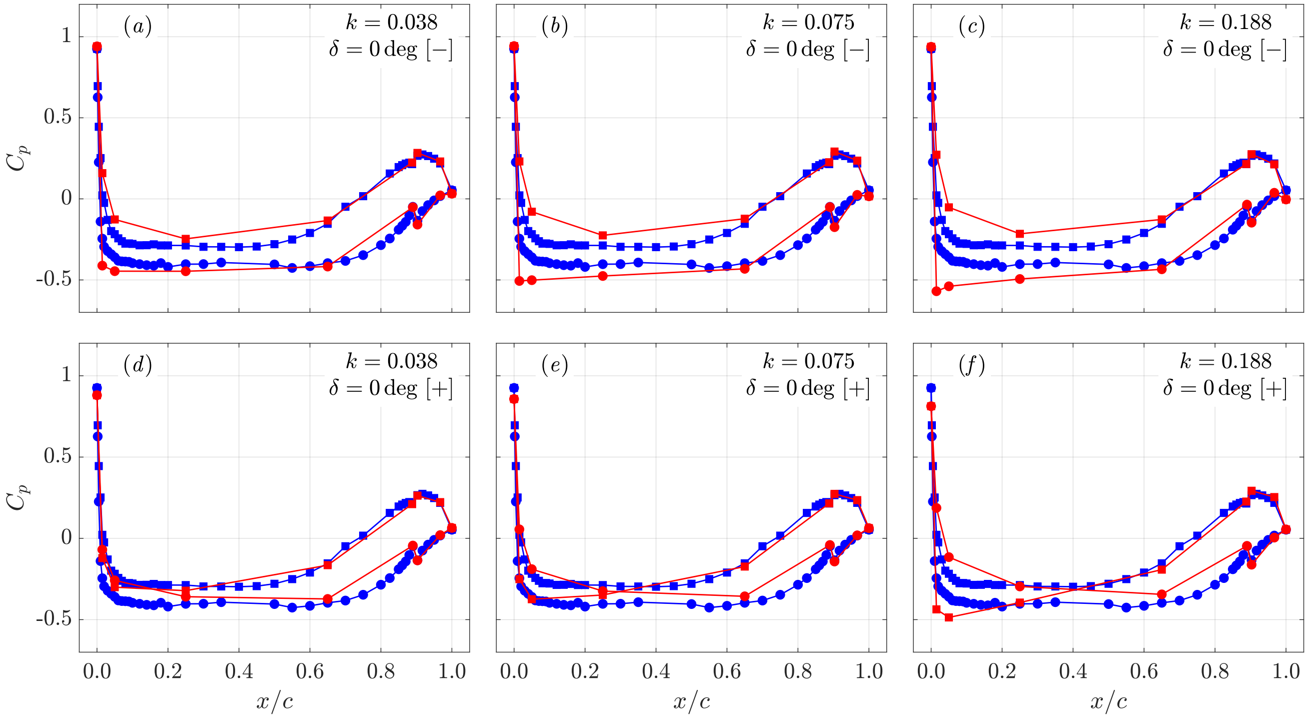

FIG. 7. Instantaneous (red) and static (blue) pressure coefficient C_p distributions at $\alpha = 0°$ along the airfoil midsection over the pressure side (■) and suction side (●). The $[-]$ and $[+]$ symbols in the legend denote the moment at $\delta = 0°$ during the flap upstroke ($(a) - (c)$) and downstroke ($(d) - (f)$), respectively. The results are presented for three reduced frequencies $k = 0.038, 0.075, 0.188$ with the same mean pitch angle $\delta_0 = 0°$ and pitch amplitude $\delta_1 = 25°$.

presented test cases have the same mean pitch angle $\delta_0 = 0°$ and pitch amplitude $\delta_1 \approx 25°$. The static pressure distribution, shown in blue, differs from the instantaneous ones in red at both the upstroke and the downstroke. The instantaneous pressure fluctuations are larger in magnitude towards the leading edge. On the upstroke, when the flap pitches from positive to negative angles, the time-lag effect leads to a fuller C_p distribution and thus higher ΔC_p, and subsequently C_L, compared to the steady case. The opposite effect is present on the downstroke, where a reduced ΔC_p (and thus C_L) compared to the steady case is observed. At high reduced frequencies, as in Fig. 7(*f*) with $k = 0.188$, the time lag even causes cross-over in the pressure distribution and thus, an increase in the airfoil pitching moment C_m. These observations are consistent with previously reported results in the literature.

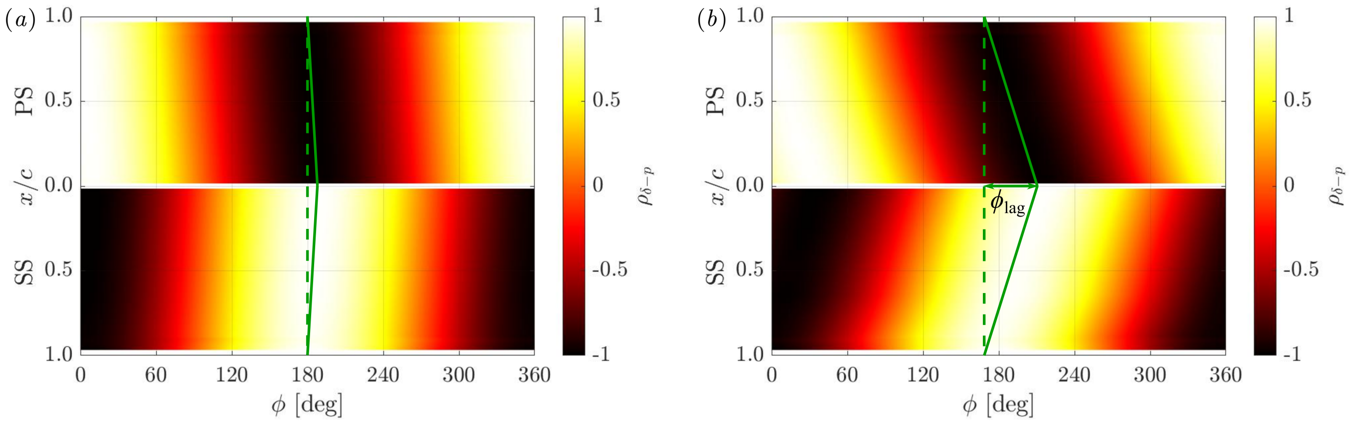

FIG. 8. Cross correlation coefficient $\rho_{\delta-p}$ distributions of the flap angle and the surface pressures at $\alpha = 0°$ with $\delta_0 = 0°$, $\delta_1 = 25°$ for (a) $k = 0.038$ and (b) $k = 0.188$. The green solid line denotes the perfect correlation (anti-correlation) between the flap motion and the surface pressures.

To better understand the time-lag, we examine the cross-correlation coefficient between the flap deflection angle and the local surface pressure, defined as

$$\rho_{\delta-p}(\tau) = \frac{\frac{1}{T}\int_0^T \left(\delta(t^*) - \overline{\delta}\right)\left(C_p(t^* + \tau) - \overline{C}_p\right) dt^*}{\sigma(\delta)\sigma(C_p)}\,, \tag{13}$$

where τ is the time-delay, T is the pitching period, σ is the standard deviation, and $\overline{}$ denotes the time averaging operator. The cross-correlation coefficient $\rho_{\delta-p}$ distributions are presented in Fig. 8 for two reduced frequencies $k = 0.038$ and $k = 0.188$, respectively. The results are presented as a function of the phase-delay $\phi = 2\pi\frac{\tau}{T}$. PS and SS denote the pressure side and the suction side of the airfoil, respectively. From the definition of $\rho_{\delta-p}$ and as can be seen in Fig. 8, $\rho_{\delta-p}$ is in-phase with the flap motion ($\phi = 0°$) at the trailing edge pressure side and is in opposite phase with the flap ($\phi = 180°$) on the trailing edge suction side. This perfect correlation (anti-correlation) gradually shifts away from the flap trailing edge towards the airfoil leading edge. The shift is marked with a solid green line across both the pressure and suction sides. It illustrates the phase (or time) lag, which increases with distance upstream as the information requires more time to reach further distances upstream of the flap. Evidently, the phase-lag increases with increasing reduced frequency, as observed when comparing Fig. 8(a) and (b). Quantifying the phase-lag at the airfoil leading edge with ϕ_{lag} yields an increase from $\phi_{\text{lag}} \approx 8°$ at $k = 0.038$ to $\phi_{\text{lag}} \approx 42°$ at $k = 0.188$. Note that, even though the maximum phase lag ϕ_{lag} appears to increase linearly with k for the two illustrated cases, this is not the case in general. In fact, ϕ_{lag} behaves similarly to the airfoil lift, which is an integrated quantity of the surface pressure and whose phase response is given in Fig. 5(a) for select experimental test cases.

A similar trend is observed in the differential pressure coefficient distributions ΔC_p, which is the pressure difference between the airfoil suction side and the pressure side. Distributions of ΔC_p are shown in Fig. 9 for the same two test cases as in Fig. 8 over one period of harmonic flap actuation. As with the flap angle–pressure correlation coefficient, the same phase shift of 8° and 42° at the leading edge for $k = 0.038$ and $k = 0.188$, respectively, is observed.

The time lag effects are reflected in the lift coefficient distributions as dynamic hysteresis. The instantaneous lift coefficient C_L over one phase-averaged pitching period is presented in Fig. 10. The lift hysteresis is shown in Fig. 10(a) for increasing pitch amplitudes δ_1 and a constant mean pitch angle $\delta_0 = 0°$ and a constant reduced frequency $k = 0.188$, whereas Fig. 10(b) compares the lift hysteresis of six different test cases: three within the linear region of the steady airfoil lift ($\delta_0 = -5°$), and three within the separated flap region ($\delta_0 = 15°$) for quasi-constant pitch amplitude and three reduced frequencies $k = 0.075, 0.188$, and 0.754. Expectedly, the increase in pitch amplitude δ_1 is associated with a growth of the hysteresis loops (c.f. Fig. 10(a)). We note the bend in the loops between $\delta = 5°$ and $\delta = 15°$ on the downstroke, where the flap separates. The comparison of the lift hysteresis loops at similar pitch angle and pitch amplitude for increasing reduced frequencies reveals a different aspect of the time lag effect. Lift hysteresis curves at higher pitch frequencies exhibit a tilt with a reduced mean slope, as shown in Fig. 10(b). Hence, the pitching flap yields a smaller lift gain $\Delta C_L/\delta_1$ with increasing reduced frequency, in agreement with the frequency response shown in Fig. 5(b). This reduction translates into a decreased authority of the trailing edge flap for lift control. This effect is also present for the $\delta_0 = 15°$ cases, albeit to a smaller extent as the separated flap possesses a reduced influence on the flow. It is worth noting the clockwise rotation direction of the hysteresis loop for the $k = 0.754$ case pitching

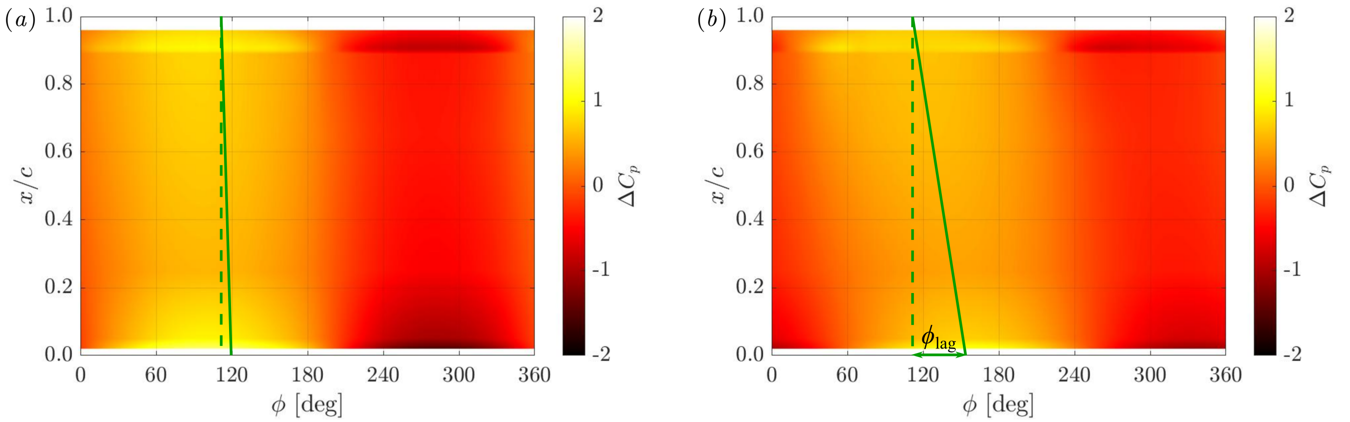

FIG. 9. Differential pressure coefficient distributions ΔC_p for one period of harmonic flap actuation at $\alpha = 0^\circ$ with $\delta_0 = 0^\circ$, $\delta_1 = 25^\circ$ for (a) $k = 0.038$ and (b) $k = 0.188$.

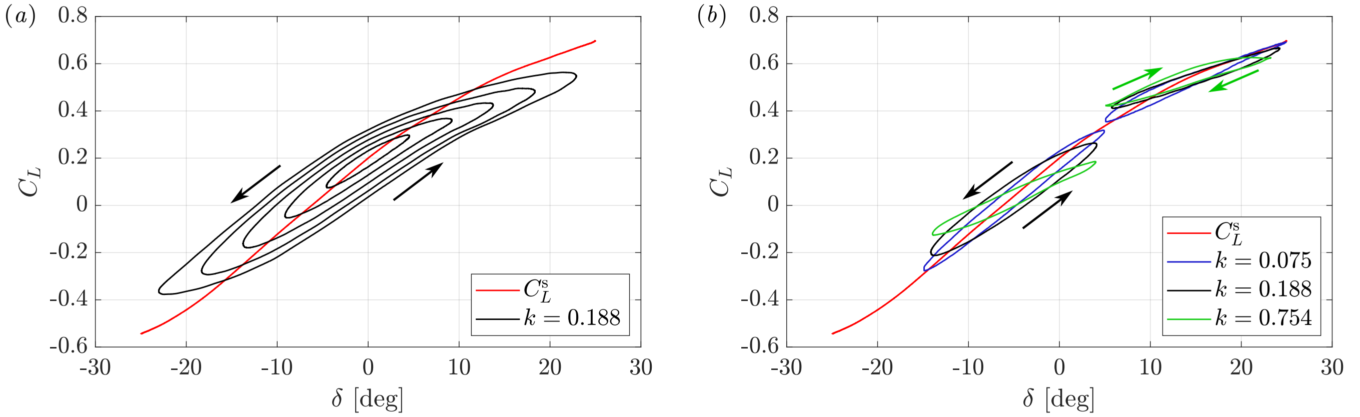

FIG. 10. The instantaneous lift coefficient C_L over one phase-averaged pitching period. (a) The lift hysteresis for an increasing pitch amplitude δ_1 and a constant mean pitch angle $\delta_0 = 0^\circ$ and a constant reduced frequency $k = 0.188$. (b) The lift hysteresis of six different test cases: three within the linear region of the steady airfoil lift ($\delta_0 = -5^\circ$), and three within the separated flap region ($\delta_0 = 15^\circ$) for quasi-constant pitch amplitude and three reduced frequencies $k = 0.075, 0.188$, and 0.754.

about $\delta_0 = 15^\circ$, which is in the opposite counterclockwise direction to the other presented cases.

Following these observations, we attempt to quantify the lift hysteresis characteristics (magnitude, tilt, rotation direction) and their evolution over the range of conditions. Following McCroskey's [44] definition for the pitching moment, we first define the net lift hysteresis over one pitch cycle as

$$\zeta_L = \oint C_L \, \mathrm{d}\delta \, . \tag{14}$$

To isolate the relative hysteresis effects, we normalize ζ_L by the pitching amplitude $2\delta_1$ and the corresponding steady lift difference $\Delta C_L^{\text{s}} = C_L^{\text{s}}(\delta_{\max}) - C_L^{\text{s}}(\delta_{\min})$ to obtain the net relative lift hysteresis

$$\zeta_L^* = \frac{\zeta_L}{(2\delta_1 \cdot \Delta C_L^{\text{s}})} \, , \tag{15}$$

which is presented in Fig. 11 for all test cases at the three angles of attack. ζ_L^* is thus a metric that quantifies the relative hysteresis bulk and the loop rotation, where positive value denote counterclockwise rotation and negative values clockwise rotation. The colors denote the degree of separation at steady conditions, which we quantify as

$$\Omega = \min \left\{ \frac{\max\left\{\delta_{\max} - \delta_{\text{sep}}^{+}, 0\right\} + \max\left\{\delta_{\text{sep}}^{-} - \delta_{\min}, 0\right\}}{\delta_{\max} - \delta_{\min}}, 1 \right\} \tag{16}$$

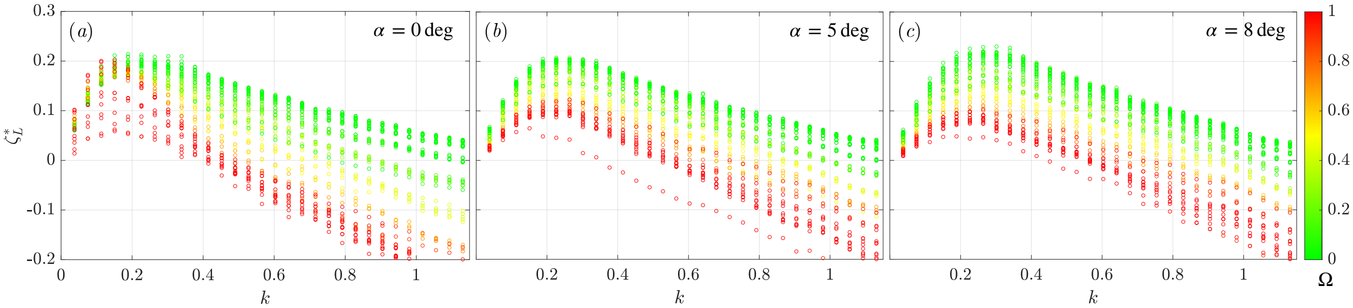

FIG. 11. Relative net hysteresis ζ_L^* distributions for a range of reduced frequencies k for (a) $\alpha = 0\,^\circ$, (b) $\alpha = 5\,^\circ$, and (c) $\alpha = 8\,^\circ$. Measurement points are color-coded by the respective degree of separation Ω, where green indicates a fully-attached flow on both sides of the flap, and red indicates a fully-separated flow over one side of the flap.

where δ_{sep}^+ and δ_{sep}^- delimit the attached flow region under steady conditions. Eq. (16) yields $\Omega = 1$ for a fully separated flow over one side of the flap over one pitching period, and $\Omega = 0$ for a fully-attached flow over both sides. We acknowledge the existence of other metrics to quantify the degree of separation (e.g., [45]). However, for the current configuration with a relatively small flap and as confirmed by the results, Ω is deemed sufficiently accurate. As Fig. 11 shows, ζ_L^* saturates at ≈ 0.22 around $0.2 \leq k \leq 0.3$ for all three angles of attack, and continuously decreases thereafter until it becomes negative for sufficiently high reduced frequencies. Hence, the net relative lift hysteresis exhibits an upper limit that is independent of the airfoil angle of attack, at least in the linear range. Except for a few cases at $\alpha = 0^\circ$ affected by the gust generator airfoil wake, larger relative net hysteresis ζ_L^* is reached for more attached flow conditions over the flap (lower Ω). We reiterate that these wake effects take place despite the gust generator airfoil 'parked' at zero degree incidence angle throughout the current measurements. More details on the gust generator wake are provided in Part II of this series.

With increasing pitching frequency, the relative net hysteresis eventually becomes negative indicating a reversal in the hysteresis loop direction, as previously presented in Fig. 10(b) and as reported in some literature (e.g., [31]). This reversal is simply phase opposition, which is attributed to the noncirculatory terms beginning to dominate the flow response. The reversal takes place earlier with increasing level of separation, i.e., for larger Ω. For example, a test case with $\Omega = 1$ in Fig. 11(a) reaches phase lead at $k \approx 0.43$, whereas a fully attached case with $\Omega = 0$ does not show phase opposition within the measured frequency range.

We reiterate that large negative ζ_L^* values denote large net relative hysteresis with clockwise rotation. Hence, with larger reduced frequencies, smaller ζ_L^* values are reached, which in absolute terms, reach similar magnitude to the positive maxima. Based on the observed trends, a possible smaller net relative hysteresis at higher k (beyond the measured range) is likely.

The third hysteresis loop characteristic is tilting, which we quantify by the relative lift hysteresis tilt parameter

$$\lambda_L^* = \frac{(\mathrm{d}C_L/\mathrm{d}\delta)}{\Delta C_L^s/(2\delta_1)}\,, \tag{17}$$

where $\mathrm{d}C_L/\mathrm{d}\delta$ is identified from the slope of a simple linear fit through the hysteresis loop. The relative tilt λ_L^* distributions for a range of reduced frequencies k for the three angles of attack are presented in Fig. 12. Similarly to Fig. 11, the measurement points are color-coded by the respective degree of separation Ω, where green indicates a fully attached flow on both sides of the flap, and red indicates a fully separated flow over one side of the flap. Except for a few cases at $\alpha = 0\,^\circ$, the evolution of λ_L^* is similar among the three angles of attack. The few exceptions at $\alpha = 0\,^\circ$ are caused by interference from the gust generator airfoil wake. This is confirmed by comparing the current results to those of a previous measurement campaign [33] without the mechanism. As the figure shows, the relative tilt is also dependent on the state of separation. Mostly attached test cases (Ω close to zero) exhibit a larger relative tilt than the separated cases (Ω close to one) that continues to decrease over the entire measurement range. On the other hand, the λ_L^* distributions of the mostly separated cases initially decrease with higher k before they subsequently increase at a slower rate. It is not possible to predict how the tilt further evolves beyond the current measurement range. A possible return to initial tilt values can not be excluded. Interestingly, the onset of the slope reversal coincides with the phase opposition frequency identified from the ζ_L^* distributions in Fig. 11. In other words, the loop reversal frequency is also the tilt inflection point.

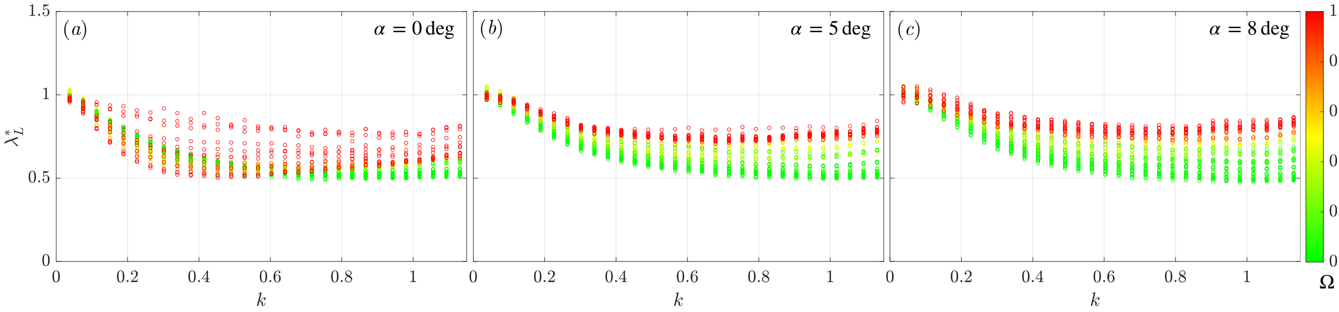

FIG. 12. Relative tilt λ_L^* distributions for the current range of reduced frequencies k for (a) $\alpha = 0\,^\circ$, (b) $\alpha = 5\,^\circ$, and (c) $\alpha = 8\,^\circ$. Measurement points are color-coded by the respective degree of separation Ω, where green indicates a fully-attached flow on both sides of the flap, and red indicates a fully-separated flow over one side of the flap.

C. Unsteady lift models

The lift coefficient models presented in section III are now assessed and compared. This assessment is aimed to evaluate the models' robustness at different operating conditions, to shed light on the lift dynamics, and to evaluate the models' suitability for the control strategy detailed in Part II of this series. For brevity and clarity, we present only results for $\alpha = 0\,^\circ$. Similar conclusions can be drawn at the other two angles of attack.

The measured and modeled unsteady lift is presented in Fig. 13 for four test cases. We note that the linear model is the one derived at $\alpha = 0\,^\circ$ and linearized around $\delta = 0\,^\circ$. Two test cases with the same mean pitch angle $\delta_0 = 0°$ and pitch amplitude $\delta_1 \approx 25°$ are compared at two different reduced frequencies, as shown in Figs. 13(a)-(b). Similarly, Figs. 13(c)-(d) compares two test cases, but with the same reduced frequency $k = 0.754$ and pitching amplitude $\delta_1 \approx 10°$ at mean pitch angles $\delta_0 = 0°$ and 15°. The four test cases are specifically selected to highlight the models' accuracy as well as their limitations. The general lift distribution is well reproduced by both models, as shown in Fig. 13(a). The overall hysteresis loop including the sharp turning at $\delta = 25°$ for this low pitch frequency case is well reproduced by the nonlinear model. Unsurprisingly, the linear model is not capable of reproducing the nonlinear dynamics at $\delta > \delta^+_{\mathrm{sep}} \approx 5°$. This is also reflected in Fig. 13(b), where the lift distributions at $k = 0.188$ for the measured data and the two model predictions are shown. Both models account for the increased net hysteresis loop size with higher frequencies, and thus the increased phase delay of the flow. However, the linear model deviates from the reference data, as nonlinear effects associated with the flap separation start to take effect.

This trend extends to higher reduced frequencies. Lift distributions of the two test cases already shown in Fig. 10(b) with $k = 0.754$ is presented in Figs. 13(c)-(d). The performance of models at higher pitching frequencies without flap separation is shown in Fig. 13(c). The hysteresis loop is well reproduced by both the nonlinear and the linear models, which also correctly predict the tilt. In Fig. 13(d), the models are applied to a fully-separated test case. As can be seen, the nonlinear model deviates from the reference lift on the upstroke when the flap is separated, and yields a smaller ζ_L^* compared to the reference measurements. Nonetheless, the model accurately predicts the hysteresis loop reversal to a clockwise direction. The performance loss is an expected limitation of the model, since all components simulating the dynamic stall have been simplified. On the other hand, the linear model fails to predict both the steady as well as unsteady lift components. This is again expected since the model is linearized at $\delta = 0°$ in the linear lift range and is deployed at $\delta = 15°$, where both static and dynamic stall is present. For the range of frequencies studied, the linear model also fails to predict phase opposition, and hence hysteresis loop direction reversal.

A more general assessment of the models is achieved by examining the relative net hysteresis ζ_L^*. The net relative hysteresis distributions from measured data is compared to those predicted by the two models in Fig. 14. The results for attached test cases with $\Omega = 0$ are shown in Fig. 14(a). Here, the predicted ζ_L^* by the nonlinear model matches the reference distribution accurately, whereas the linear model slightly under-predicts for $k > 0.2$. Conversely, for test cases with a separated flap ($\Omega = 1$) shown in Fig. 14(b), both the linear and nonlinear models fail to accurately predict the lift hysteresis. The nonlinear model still outperforms the linear model, which heavily over-predicts ζ_L^* across the frequency range. The inability to capture dynamic stall is expected since both model structure is specifically simplified to ignore it.

In this project, we aim for gust mitigation at a single angle of attack $\alpha = 0\,^\circ$ and at (mainly) a reference flap angle $\delta = 0\,^\circ$. As detailed in Part II of this series, the flap requirements to counter the largest generated gusts in the facility are within the range of pitching conditions used to train the linear models, i.e., $\delta^-_{\mathrm{sep}} = -20\,^\circ \leq \delta \leq \delta^+_{\mathrm{sep}} = 5\,^\circ$ and $k < 0.72$, which demonstrated good predictive capabilities within this range. In addition, linear models are well-suited for a multitude of powerful yet simple linear control techniques with low latency. Therefore, despite their

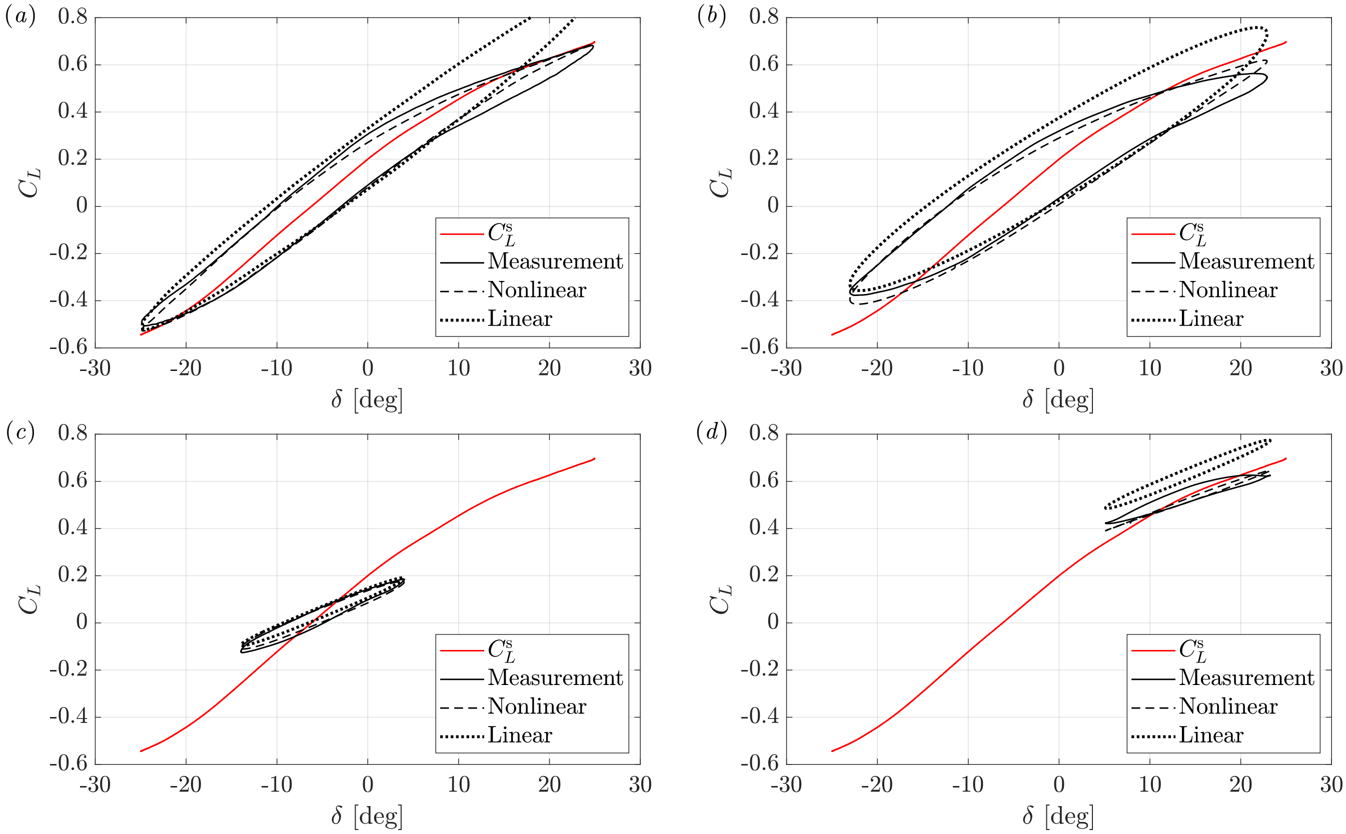

FIG. 13. The measured (—) and the modeled (−− and ..) unsteady lift for four test cases. Two test cases have the same mean pitch angle $\delta_0 = 0^\circ$ and pitch amplitude $\delta_1 \approx 25^\circ$ at two different reduced frequencies (*a*) $k = 0.075$ and (*b*) $k = 0.188$. Two test cases have the same reduced frequency $k = 0.754$ and pitching amplitude $\delta_1 \approx 10^\circ$ at mean pitch angle (*c*) $\delta_0 = 0^\circ$ and (*d*) $\delta_0 = 15^\circ$.

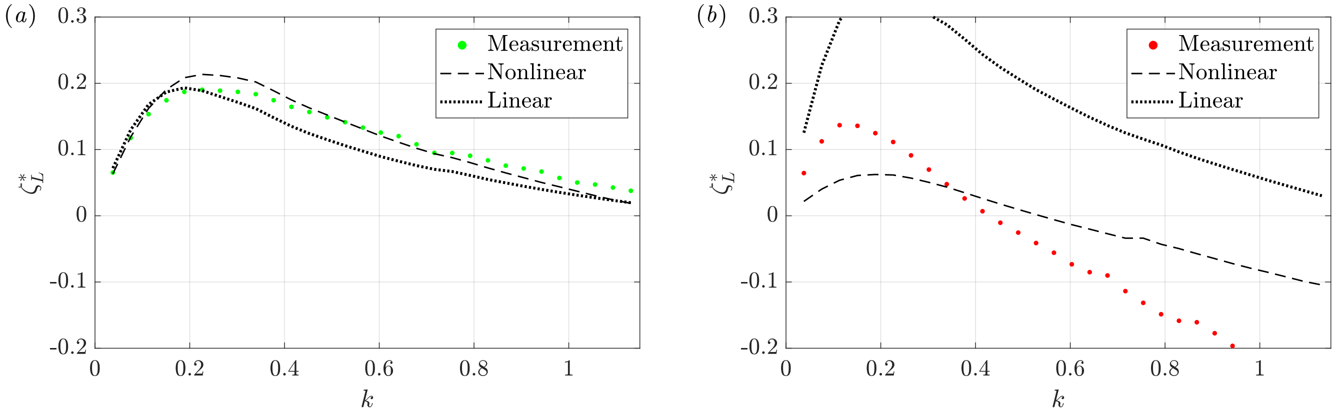

FIG. 14. Relative net hysteresis ζ_L^* distributions for a range of reduced frequencies k at $\alpha = 0^\circ$ for (*a*) fully attached, and (*b*) fully separated test cases over the flap. The symbol ● denotes measured data, whereas (−−) and (..) mark the nonlinear and linear models, respectively.

poorer performance over the entire range compared to the nonlinear model, we choose the linear models for the gust mitigation strategy detailed in Part II.

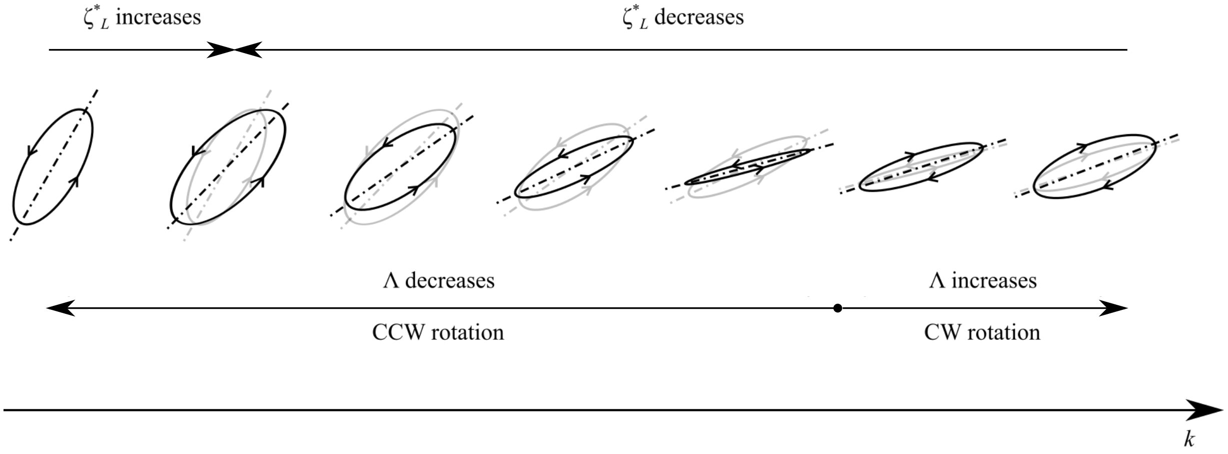

FIG. 15. Evolution of the hysteresis loop for the current range of reduced frequency k. The schematic illustrates the relative net hysteresis initial increase followed by the subsequent continuous decrease with increasing pitching frequency. Also illustrated is the relation between the hysteresis loop tilt and rotation direction, where phase opposition delimits the reversal of the slope trend.

V. CONCLUSIONS

In this study, we perform a comprehensive experimental study on an airfoil with a pitching flap at a chord Reynolds number $Re_c = 1.8 \cdot 10^6$. The measurements distinguish themselves from the current state of the art in the Reynolds number used and the broad experimental pitching conditions tested. The data are employed to characterize the lift hysteresis evolution and to identify a suitable model for a closed-loop control strategy.

We characterize the lift hysteresis by introducing and analyzing two metrics: the net relative lift hysteresis ζ^*_L, and the relative lift hysteresis tilt λ^*_L. Evaluation of the ζ^*_L distributions reveal a maximum at ≈ 0.22 around $0.2 \leq k \leq 0.3$ for all three angles of attack. Larger relative net hysteresis ζ^*_L is reached for more attached flow conditions over the flap, reflecting higher authority to control the flow. With increasing pitching frequency, the relative net hysteresis decreases and eventually becomes negative, corresponding to a reversal in the hysteresis loop direction. This phase lead is attributed to the noncirculatory terms beginning to dominate the flow response. The phase-opposition takes place earlier with increasing level of separation.

The second metric we introduce to quantify the hysteresis is the relative lift hysteresis tilt λ^*_L. Similar to ζ^*_L, the λ^*_L distributions at the three angles of attack show similar trends. The relative tilt is also dependent on the state of separation. The attached cases exhibit a larger relative tilt than the separated ones with a steady decrease with increasing reduced frequency within the measured range. For separated conditions over the flap, the λ^*_L distributions initially decrease with higher k before they increase although at a slower rate. The onset of this slope reversal coincides with the phase opposition frequency identified from the ζ^*_L distributions.

Based on the preceding conclusions, we schematically summarize the evolution of the hysteresis loop in Fig. 15. The schematic shows the relative net hysteresis initial increase followed by the continuous decrease with increasing pitching frequency. Also illustrated is the relation between the hysteresis loop tilt and its rotation direction, where phase opposition delimits the reversal of the slope trend. Comparable behavior can be assumed for other pitching flaps and even airfoils when they are operating below the large dynamic stall range. The two-pronged characterization of the lift hysteresis constitute a new promising approach to quantify the unsteady aerodynamic behavior beyond the reported conditions and of other immersed bodies.

One main objective of this study is to perform model-based closed-loop control to mitigate gust effects, which requires an accurate and – preferably simple – model of the lift coefficient response to flap motion. Two different modeling approaches are followed. The first builds on the ONERA model [23] with a discarded dynamic stall component. Despite this simplification, the model is shown to accurately model the lift coefficient over broad pitching conditions. Discrepancies are only observed at high mean pitch angles for cases with large dynamic stall. Despite its accuracy, the nonlinear model is not ideal for a closed-loop control strategy.

The second modeling approach constructs three linear models with two poles and two zeros in the frequency domain using a data subset at a single mean pitch angle $\delta_0 = 0°$, and a range of pitching amplitudes $\delta_1 < 10°$, and reduced frequencies $k < 0.72$. This parameter range is within the requirements to counter the generated gusts. Within this range, the models exhibit good performance similar to that of the nonlinear model. Considering its additional amenability to closed-loop control, the linear models are selected for the gust-mitigation strategy. We conjecture that linear models could be useful for a range of similar applications, bypassing the complexity associated with nonlinear models in the control loop.

ACKNOWLEDGMENTS

The authors gratefully acknowledge the funding of the state of Lower-Saxony and the Technische Universität Braunschweig. SLB acknowledges funding support from the Army Research Office (ARO W911NF-19-1-0045).

[1] N. H. Al-Battal, D. J. Cleaver, and I. Gursul, Lift reduction by counter flowing wall jets, Aerospace Science and Technology **78**, 682 (2018).

[2] D. R. Williams and R. King, Alleviating unsteady aerodynamic loads with closed-loop flow control, AIAA Journal **56**, 2194 (2018).

[3] G. He, J. Deparday, L. Siegel, A. Henning, and K. Mulleners, Stall delay and leading-edge suction for a pitching airfoil with trailing-edge flap, AIAA Journal **58**, 5146 (2020).

[4] L. Prandtl, Über die Entstehung von Wirbeln in der idealen Flüsssigkeit, mit Anwendung auf die Tragflügeltheorie und andere Aufgabe, Vorträge aus dem Gebiete der Hydro-und Aerodynamik (Innsbruck 1922) , 18 (1924).

[5] W. Birnbaum, Der Schlagflügelpropeller und die kleinen Schwingungen elastisch befestigter Tragflügel, Zeitschrift für Flugtechnik und Motorluftschiffahrt **15**, 128 (1924).

[6] H. Wagner, Über die Entstehung des dynamischen Auftriebes von Tragflügeln, ZAMM - Zeitschrift für Angewandte Mathematik und Mechanik **5**, 17 (1925).

[7] T. Theodorsen, *General Theory of Aerodynamic Instability and the Mechanism of Flutter*, Report 496 (National Advisory Committee for Aeronautics, 1935).

[8] T. H. von Karman and W. R. Sears, Airfoil theory for non-uniform motion, Journal of the Aeronautical Sciences **5**, 379 (1938).

[9] R. T. Jones, *Operational treatment of the nonuniform-lift theory in airplane dynamics*, Tech. Rep. 667.

[10] R. Vepa, On the use of padé approximants to represent unsteady aerodynamic loads for arbitrarily small motions of wings, in *AIAA Paper 76-17* (1976).

[11] M. Zakaria, H. Taha, and M. Hajj, Measurement and modeling of lift enhancement on plunging airfoils: A frequency response approach, Journal of Fluids and Structures **69**, 187 (2017).

[12] M. V. OL, A. Altman, J. D. Eldredge, D. J. Garmann, and Y. Lian, Résumé of the AIAA FDTC low Reynolds number discussion group's canonical cases, AIAA Paper 2010-1085, 48th Aerospace Sciences Meeting (2010).

[13] J. D. Eldredge and A. R. Jones, Leading-edge vortices: mechanics and modeling, Annual Review of Fluid Mechanics **51**, 75 (2019).

[14] K. Ramesh, A. Gopalarathnam, K. Granlund, M. V. Ol, and J. R. Edwards, Discrete-vortex method with novel shedding criterion for unsteady aerofoil flows with intermittent leading-edge vortex shedding, Journal of Fluid Mechanics **751**, 500 (2014).

[15] D. Darakananda and J. D. Eldredge, A versatile taxonomy of low-dimensional vortex models for unsteady aerodynamics, Journal of Fluid Mechanics **858**, 917 (2019).

[16] J. D. Eldredge, *Mathematical modeling of unsteady inviscid flows* (Springer, 2019).

[17] S. L. Brunton and C. W. Rowley, Empirical state-space representations for Theodorsen's lift model, Journal of Fluids and Structures **38**, 174 (2013).

[18] S. L. Brunton, S. T. M. Dawson, and C. W. Rowley, State-space model identification and feedback control of unsteady aerodynamic forces, Journal of Fluids and Structures **50**, 253 (2014), arXiv:1401.1473.

[19] H. Snel, Heuristic modelling of dynamic stall characteristics, in *European Wind Energy Conference* (Dublin Castle, Ireland, 1997) pp. 429–433.

[20] M. Goman and A. Khrabrov, State-space representation of aerodynamic characteristics of an aircraft at high angles of attack, Journal of Aircraft **31**, 1109 (1994).

[21] D. R. Williams, F. Reißner, D. Greenblatt, H. Müller-Vahl, and C. Strangfeld, Modeling lift hysteresis on pitching airfoils with a modified Goman–Khrabrov model, AIAA Journal **55**, 403 (2017).

[22] G. Sedky, A. R. Jones, and F. D. Lagor, Lift regulation during transverse gust encounters using a modified Goman–Khrabrov model, AIAA Journal **58**, 3788 (2020).

[23] K. W. McAlister, D. Petot, and O. Lambert, *Application of the ONERA Model of Dynamic Stall*, Tech. Rep. 2399 (1984).

[24] H. Babinsky, R. J. Stevens, A. R. Jones, L. P. Bernal, and M. V. Ol, Low Order Modelling of Lift Forces for Unsteady Pitching and Surging Wings, in *54th AIAA Aerospace Sciences Meeting* (American Institute of Aeronautics and Astronautics, San Diego, California, USA, 2016).

[25] M. S. Hemati, S. T. M. Dawson, and C. W. Rowley, Parameter-varying aerodynamics models for aggressive pitching-response prediction, AIAA Journal , 1 (2016).

[26] T. Colonius, C. W. Rowley, G. Tadmor, D. Williams, K. Taira, W. Dickson, M. Gharib, and M. Dickinson, Closed-loop

control of leading-edge and tip vortices for small UAV, in *Conference on Active Flow Control, DFG, Berlin*, Vol. 2729 (2006).

[27] K. Taira, W. B. Dickson, T. Colonius, M. H. Dickinson, and C. W. Rowley, Unsteadiness in flow over a flat plate at angle-of-attack at low Reynolds numbers., AIAA Paper 2007-710, 45th Aerospace Sciences Meeting (2007).

[28] W. Kerstens, J. Pfeiffer, D. Williams, R. King, and T. Colonius, Closed-loop control of lift for longitudinal gust suppression at low Reynolds numbers, AIAA Journal **49**, 1721 (2011).

[29] P. F. Lorber and F. O. Carta, Airfoil dynamic stall at constant pitch rate and high Reynolds number, Journal of Aircraft **25**, 548 (1988).

[30] J. Panda and K. B. M. Q. Zaman, Experimental investigation of the flow field of an oscillating airfoil and estimation of lift from wake surveys, Journal of Fluid Mechanics **265**, 65 (1994).

[31] N. Hariharan and J. G. Leishman, Unsteady aerodynamics of a flapped airfoil in subsonic flow by indicial concepts, Journal of Aircraft **33**, 855 (1996).

[32] D. R. Williams, X. An, S. Iliev, R. King, and F. Reißner, Dynamic hysteresis control of lift on a pitching wing, Experiments in Fluids **56**, 112 (2015).

[33] J. Pohl, R. Semaan, and A. R. Jones, Dynamic lift measurements on an airfoil with periodic flap motion at high Reynolds number, in *AIAA Scitech 2019 Forum* (American Institute of Aeronautics and Astronautics, San Diego, California, 2019).

[34] J. Pohl and R. Semaan, Quantification and modeling of dynamic lift on a DLR-F15 research airfoil with active trailing-edge flap, in *AIAA Scitech 2020 Forum* (American Institute of Aeronautics and Astronautics, Orlando, FL, 2020).

[35] R. Semaan and V. Yadav, Scout: signal correction and uncertainty quantification toolbox in matlab, SoftwareX **11**, 100474 (2020).

[36] S. Sarkar and H. Bijl, Nonlinear aeroelastic behavior of an oscillating airfoil during stall-induced vibration, Journal of Fluids and Structures **24**, 757 (2008).

[37] P. K. Chaviaropoulos, Flap/lead–lag aeroelastic stability of wind turbine blade sections, Wind Energy **2**, 99 (1999).

[38] J. G. Leishman, Unsteady lift of a flapped airfoil by indicial concepts, Journal of Aircraft **31**, 288 (1994).

[39] J. G. Leishman, *Principles of Helicopter Aerodynamics*, Cambridge Aerospace Series No. 12 (Cambridge University Press, Cambridge ; New York, 2000).

[40] H. E. Taha and A. S. Rezaei, Viscous extension of potential-flow unsteady aerodynamics: the lift frequency response problem, Journal of Fluid Mechanics **868**, 141 (2019).

[41] H. E. Taha and A. S. Rezaei, On the high-frequency response of unsteady lift and circulation: a dynamical systems perspective, Journal of Fluids and Structures **93**, 102868 (2020).

[42] A. A. Ozdemir and S. Gumussoy, Transfer function estimation in system identification toolbox via vector fitting, IFAC-PapersOnLine **50**, 6232 (2017).

[43] T. Shaqarin, P. Oswald, B. N. Noack, and R. Semaan, Drag reduction of a D-shaped bluff-body using linear parameter varying control, Accepted for publication in Physics of Fluids (2021).

[44] W. J. McCroskey, Unsteady Airfoils, Annual Review of Fluid Mechanics **14**, 285 (1982).

[45] R. L. Simpson, Turbulent boundary-layer separation, Annual Review of Fluid Mechanics **21**, 205 (1989).